

A 1.4 GHz Survey of the Southern ELAIS Region

C. Gruppioni¹*, P. Ciliegi^{2,3}, M. Rowan-Robinson¹, L. Cram⁴, A. Hopkins⁴,
 C. Cesarsky⁵, L. Danese⁶, A. Franceschini⁷, R. Genzel⁸, A. Lawrence⁹,
 D. Lemke¹⁰, R.G. McMahon², G. Miley¹¹, S. Oliver¹, J-L. Puget¹², B. Rocca-
 Volmerange^{13,12}

¹ *Astrophysics Group, Imperial College London, Prince Consort Road, London SW7 2BZ, U.K.*

² *Institute of Astronomy, Madingley Road, Cambridge, CB3 0HA*

³ *Osservatorio Astronomico di Bologna, via Zamboni 33, Bologna, I-40126, Italy*

⁴ *School of Physics, University of Sydney, NSW, 2006, Australia*

⁵ *Service d'Astrophysique, Saclay, 91191, Gif-sur-Yvette, Cedex, France*

⁶ *SISSA, Via Beirut 2-4, Trieste, Italy*

⁷ *Osservatorio Astronomico di Padova, Vicolo dell'Osservatorio 5, I-35122, Padova, Italy*

⁸ *Max-Planck-Institut für Extraterrestrische Physik, Giessenbachstrasse, D-8046, Garching bei München, Germany*

⁹ *Institute for Astronomy, University of Edinburgh, Blackford Hill, Edinburgh, EH9 3HJ*

¹⁰ *Max Plank Institute, Heidelberg, Germany*

¹¹ *Leiden Observatory, P.O. Box 9513, 2300 RA, Leiden, The Netherlands*

¹² *Institut d'Astrophysique Spatiale, Bat. 121, Université Paris XI, F-91405 Orsay Cedex, France*

¹³ *Institut d'Astrophysique de Paris, CNRS, 98 bis Bd. Arago, F-75014, Paris, France*

Accepted ?? Received ??

ABSTRACT

A deep survey of the European Large Area ISO Survey (ELAIS) field in the southern celestial hemisphere (hereinafter S1) has been carried out with the Australia Telescope Compact Array (ATCA) at 1.4 GHz. The S1 region, covering about 4 square degrees, has been also surveyed in the mid- and far-infrared (5–200 μ m) with the Infrared Space Observatory (ISO). The radio survey provides uniform coverage of the entire S1 region, with a sensitivity (5σ) of 0.4 mJy over the whole area and 0.2 mJy in the center. To this sensitivity, virtually all the radio counterparts of the far-infrared extragalactic ISO sources should be detected. This paper presents a radio sample—complete at the 5σ level—consisting of 581 sources detected at 1.4 GHz. Of these radio sources, 349 have peak flux density in the range 0.2–1 mJy, forming a new homogeneous sample of sub-mJy radio sources. Due to its size, depth and multi-waveband coverage, the sample will allow us to study in greater detail the sub-mJy radio source population.

The full catalogue will be available from <http://athena.ph.ac.uk/>

Key words: cosmology: observations – radio continuum: galaxies – infrared: galaxies – surveys – galaxies: star-burst.

1 INTRODUCTION

The European Large Area ISO Survey (ELAIS, Oliver et al. 1997; Oliver et al. 1998 in preparation) is a collaboration between 20 European institutes. It involves a deep, wide-angle survey at high galactic latitudes, at wavelengths of 6.7 μ m, 15 μ m, 90 μ m and 175 μ m with the Infrared Space Observatory (ISO). The 6.7 μ m and 15 μ m surveys were carried out with the ISO-CAM camera (Cesarsky et al. 1997) to 5σ sensitivities of \sim 0.6 and 2 mJy, respectively. The 90 μ m and 175 μ m surveys were carried out with the ISO-

PHOT photometer (Lemke et al. 1994), to a 5σ sensitivity of \sim 60–80 mJy at 90 μ m. With a sensitivity of \sim 60 mJy at 90 μ m, ELAIS will be the deepest far-infrared survey performed with ISO. The survey has detected objects 5–10 times fainter than IRAS in the 50–100 μ m range, and 20–50 times fainter than IRAS in the 10–20 μ m range. The survey is divided into 4 fields (one of which, S1, is in the southern hemisphere), and covers a total area of \sim 13 deg 2 at 15 μ m and 90 μ m, \sim 7 deg 2 at 6.7 μ m and \sim 3 deg 2 at 175 μ m.

ELAIS will allow us to study dust emission in normal galaxies and the evolution of star formation to high redshifts, testing competing scenarios for the formation of elliptical galaxies, exploring the IRAS galaxy population to

* e-mail: c.gruppioni@ic.ac.uk

higher z , and possibly unveiling new classes of objects or unexpected phenomena. Since dust plays an important role in most of these goals, and since many of the thousands of galaxies detected in the ELAIS survey will be at high redshift and probably obscured in the optical bands, radio observations will play a crucial role in assessing the reliability of the ELAIS source list and in facilitating source identification in faint or empty optical fields. Additionally, radio data will be important in the optical identification phase because the spatial resolution of ISO is insufficient to identify unambiguously many of the faintest ISO sources. Even at 15 μm the survey resolution is ~ 10 arcsec, while at 90 μm it is almost 1 arcmin, so there are multiple optical candidates within each error box.

The three northern ELAIS fields (N1, N2 and N3) have been surveyed in the radio band (at 1.4 GHz) with the Very Large Array (VLA) down to an average flux density limit of 0.25 mJy (5σ) over a total area of 4.22 deg 2 . Details of the VLA observations and a description of the catalogue containing 867 radio sources can be found in Ciliegi et al. (1998).

In this paper we describe radio observations of the ELAIS field located in the southern celestial hemisphere, S1. This field, centered at $\alpha(2000) = 00^h 34^m 44.4^s$, $\delta(2000) = -43^\circ 28' 12''$, covers an area of the sky of about $2^\circ \times 2^\circ$. We observed the whole area at 1.4 GHz with the Australia Telescope Compact Array (ATCA) in the 6-km configuration (maximum baseline length), with a resolution of 8×15 arcsec. We obtained uniform radio coverage over the whole S1 region, with sufficient sensitivity ($1\sigma \simeq 80 \mu\text{Jy}$) to detect virtually all radio counterparts of the ISO galaxies.

By combining these radio observations with the available ISO data, we will investigate the radio/far-infrared correlation (Helou, Soifer & Rowan-Robinson 1985) in star-forming galaxies to a flux density significantly deeper than that reached by IRAS. When spectral informations become available for the optical counterparts of the ISO and ATCA sources in the field, we will investigate the trivariate IR-radio-optical luminosity function and its evolution. This study will be of fundamental importance for interpreting the source counts at different wave-bands and for elucidating contributions from different classes of objects. Moreover, we will be able to determine the influence of obscuration on the inference of the star-formation rate, and to constrain the star formation history of the Universe to $z \simeq 1.0\text{--}1.5$ with two complementary samples, selected in the infrared and radio, within the same volume of the Universe (see Cram et al. 1998; Oliver, Gruppioni & Serjeant 1998).

The radio sample is also important in its own right, since it constitutes one of the largest homogeneous samples of sub-mJy radio sources, whose nature is still uncertain. Previous work has suggested that the sub-mJy radio source population is composed largely of star-burst galaxies at moderate redshifts (i.e. Windhorst et al. 1985; Benn et al. 1993). However, there is little information about the nature and the true redshift distribution of the sub-mJy population, because only a small fraction of them have been optically identified and have measured redshifts (Benn et al. 1993; Rowan-Robinson et al. 1993). Although it is commonly believed that most of the sub-mJy radio sources are associated with star-forming galaxies, recent extensions to fainter optical magnitudes (and higher identification percentages)

hint strongly at an increasing fraction of early-type galaxies (Gruppioni, Mignoli & Zamorani 1998). This suggestion, together with apparently discordant results from optical identifications of even fainter μJy radio samples (Windhorst et al. 1995; Hammer et al. 1995; Richards et al. 1998) complicate the picture. The ATCA survey in the ELAIS field S1, together with the VLA surveys of the northern fields N1, N2 and N3 (Ciliegi et al. 1998) will shed new light on the sub-mJy population and its connection to the faint blue and infrared star-burst galaxies. The sensitivity, areal coverage and multi-wavelength character (optical, near-, mid- and far-infrared and radio) of the ELAIS project will ensure that it makes an important contribution to all of these problems.

In section 2 of the paper we describe the radio observations. Section 3 discusses the data reduction strategy and section 4 presents the source catalogue. In section 5 we discuss the radio source counts and present our conclusions in section 6.

2 RADIO OBSERVATIONS

2.1 Observing Strategy

By choosing an observing frequency of 1.4 GHz, we ensure a large instantaneous field of view (33 arcmin primary beam) and hence shorten the observing time necessary to cover the entire S1 area. The sensitivity is also higher for the same integration time with respect to higher available frequencies (2.4, 4.86 and 8.44 GHz). Moreover, a frequency of 1.4 GHz reveals well any recent star-formation activity, seen at this frequency as synchrotron radiation excited by supernova remnants (Condon 1992).

We observed in continuum mode with a bandwidth B of 128-MHz. The sensitivity ΔS (mJy) is

$$\Delta S = 0.0755 S_{sys} (NtB)^{-1/2} \quad (1)$$

where S_{sys} (in Jy) is the system sensibility (350 Jy at 1.4 GHz), t is the integration time (in minutes), B is the bandwidth (in MHz) and N is the number of baselines.

2.2 The Mosaic Technique

The ATCA is an east-west array which uses the earth's rotation to sample visibilities over elliptical loci in the spatial frequency (u, v) plane. Its control system allows imaging over a field or a source whose extent is larger than the primary beam by cycling through a grid of pointings on the sky, recording the visibilities for each pointing intermittently. This *mosaic observing mode* is an efficient way to obtain uniform quality imaging over a large field, and has been used to construct our survey.

The grid of pointings in the mosaic was designed to yield a homogeneous radio source sample. We aim to have a detection threshold independent of source position, and therefore require uniform noise over the area of interest. With the mosaic technique, images obtained with single pointings are combined together into a large image (mosaic) of the entire observed region. We used 'linear combination' mosaicing rather than the 'joint deconvolution' approach (described by Sault, Staveley-Smith and Brouw 1996) because the latter

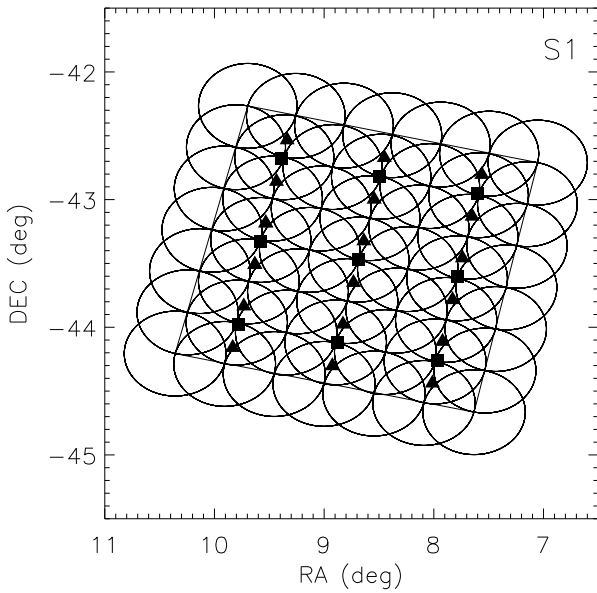


Figure 1. The sky position and orientation of the ISO S1 survey region. The outer rectangle is $2^\circ \times 2^\circ$. The filled triangles show the ISO-CAM $15\ \mu\text{m}$ pointings, while the filled squares show the ISO-PHOT $90\ \mu\text{m}$ pointings. The circles (drawn with a radius of 20 arcmin) show the ATCA mosaic pointings.

requires greater computing resources and is less suited to images dominated by compact sources. Linear combination mosaicing takes a pixel-by-pixel weighted mean of the single pointings, where the weights are determined from the primary beam response and the noise level in that pixel (Sault & Killeen 1995). The value of each pixel in the final mosaic depends on the pointing configuration and, in particular, on the grid spacing. For our survey, an optimal trade-off between uniformity of sensitivity and efficiency of telescope usage was obtained by adopting a rectangular grid of 7×7 fields, with a regular spacing between fields equal to $\theta_{FWHP}/\sqrt{2} \sim 20$ arcmin (where θ_{FWHP} is the full width at half power of the primary beam, 33 arcmin at 1.4 GHz). Figure 1 shows the sky position and orientation of the S1 region. Circles drawn with a radius of 20 arcmin show the 49 ATCA pointings.

2.3 Observations

The ATCA observations of the ELAIS field S1 were performed on the nights of 1997 June 23, 24, 26, 27 and 28, in runs of 12 hours per night. The theoretical sensitivity is $80\ \mu\text{Jy}$ (1σ) over the whole area. Since the far-infrared and radio luminosities of normal galaxies are tightly correlated (Helou, Soifer & Rowan-Robinson 1985; Condon 1992), flux-limited samples of normal galaxies selected at far-infrared and radio wavelengths at the corresponding sensitivity are nearly identical. Given a 5σ sensitivity of $60\ \text{mJy}$ for ISO observations at $90\ \mu\text{m}$, the far-infrared/radio correlation predicts that 1.4 GHz radio counterparts of the faintest ELAIS sources should be detected at a flux density a little below $0.5\ \text{mJy}$. Thus, the flux density limit reached by our observations, corresponding to $5\sigma \simeq 0.4\ \text{mJy}$, should allow us to

detect essentially all the ELAIS ISO-PHOT and most of the ISO-CAM galaxies.

To optimize (u, v) coverage we organised the observations by dividing the 49 fields in four blocks of 13 fields each and observing each block for $12\text{h} + 3\text{h}$ (one night plus one quarter of the last night). During this time the 13 fields were observed with dwell times of 20 seconds each, adding 3 minutes for observing the secondary calibrator every hour (i.e. every 15 cycles of 13 fields). The field corresponding to the center of the S1 area was visited in each block, to obtain deeper sensitivity in the central ~ 20 arcmin of the ELAIS field.

The primary flux density calibrator was PKS B1934-638, whose flux densities at different frequencies are incorporated directly in the calibration software. The primary calibrator was observed for 10 min at the beginning of each 12h observing run. The source PKS B0022-423 was used as a phase and secondary amplitude calibrator.

Before observing we checked for the presence of strong radio sources in the field, which could eventually compromise the sensitivity of the survey. Although the ELAIS S1 field was not selected with radio observations in mind, fortunately there are only a few bright radio sources within it, so that the target noise level was obtained without serious problems of confusion. The Parkes-MIT-NRAO (PMN) Southern Survey (Griffith & Wright 1993) reveals one bright radio source (PMN J0042-4413) just outside the field, with a flux density of $1.2\ \text{Jy}$ at 5 GHz. There are also one $0.4\ \text{Jy}$ and one $0.2\ \text{Jy}$ PMN source in the field, and several with lower flux densities. We have observed the whole S1 area, expecting that not more than a small part of the mosaic might be degraded by the sidelobes of strong sources in or just outside the field.

We used both receivers at 1.4 GHz, each with a bandpass of 128 MHz. Using the ATCA in this mode makes it hard to avoid strong interference in some channels for at least part of the observation, but the doubled bandwidth improves the sensitivity by a factor of $\sqrt{2}$. The optimal positioning of the bands was obtained by centering one frequency at 1.344 GHz (1.280-1.408 GHz) and the other at 1.472 GHz (1.408-1.536 GHz).

3 DATA REDUCTION

The data were analyzed with the software package MIRIAD (Multi-channel Image Reconstruction, Image Analysis and Display), which is standard software for radio-interferometric data reduction specifically adapted to the ATCA.

In particular, MIRIAD provides *multi-frequency synthesis (mfs)* algorithms (Sault & Wieringa 1994), which give the opportunity of producing images with improved (u, v) coverage by combining accurately the visibilities of individual channels. Multi-frequency synthesis may be used with the ATCA because, in continuum mode, the correlator provides a bandwidth of 128 MHz subdivided into 32 frequency channels (of 4 MHz each). The division of the wide passband into sub-channels reduces the effects of bandwidth smearing. Moreover, *mfs* fills in the (u, v) plane despite the modest number of ATCA antennas, since different observing

Figure 2. Grey scale image of the total 1.4 GHz mosaic in the ELAIS S1 field. The square region corresponds to the area observed by ISO.

frequencies produce different spatial frequency intervals Δu and Δv .

Before calibrating the data, we flagged all baselines and fringe visibilities affected by any problems encountered during the observation (such as antenna slewing intervals, interference, etc) using the tasks `BLFLAG`, `TVFLAG` and `UVFLAG`. Primary calibrator data were flagged before calibrating, and the secondary calibrator after application of the band-pass and instrumental polarization calibrations obtained from the primary calibrator. Finally, the fully calibrated single field data were flagged. Each bandpass (1.344 and 1.472 GHz) was calibrated separately, according to the standard calibration technique (Sault and Killeen 1995).

The complete imaging procedure (described in detail by Prandoni 1997) comprises imaging itself (performed with the MIRIAD task `INVERT`), and several cycles of cleaning (task `CLEAN`) and self-calibration (task `SELCAL`). The whole procedure was applied separately to each frequency to account for spectral variations of each source, since flux density dif-

ferences due to the intrinsic spectral slope could be significant over the frequency interval of 2×128 MHz. For each field we produced individual images with the same geometry and the same celestial coordinate as reference point, to be combined together into a single mosaic at the end of the reduction phase.

The images are 1200×1200 pixels square, and for each field a 2400×2400 pixels square beam was produced. An average synthesized beam of 15×8 arcsec 2 was created for all the images. Cell sizes of 2.5 arcsec per pixel were used, to obtain good re-sampling of the (u, v) plane (at least 3 pixels within each dimension of the synthesized beam). Natural weighting was used, to increase the sensitivity at the price of a decrease in spatial resolution. The images for each pointing center were then `CLEANED`. A few preliminary deconvolution iterations (performed to find the model components for the self-calibration) were followed by a self-calibration phase and then a deeper cleaning phase. This cycle was repeated twice. After subtracting from the visibility file the

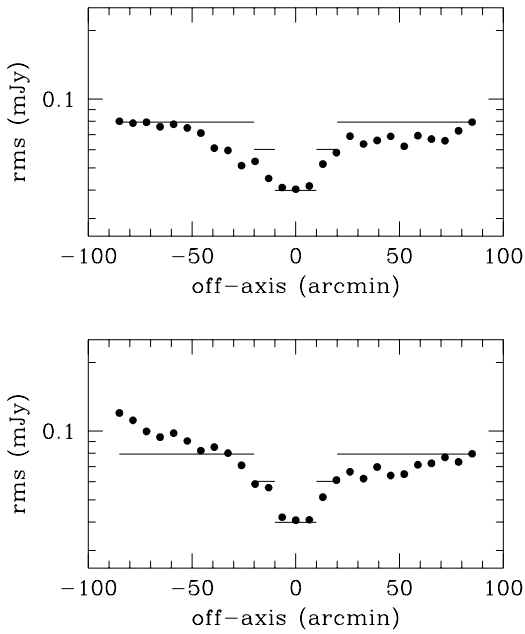


Figure 3. The rms noise as a function of distance from the field center, measured along the two diagonals of the square defined by the S1 field. *Top:* rms noise along the diagonal degraded by the sidelobes of PMNJ0042-4413; *Bottom:* rms noise along the diagonal not affected by the presence of the strong radio source. The solid lines (corresponding to 1σ rms noise values of 80, 60 and 40 μJy for $r > 20$ arcmin, $10 < r < 20$ arcmin, and $r < 10$ arcmin, respectively) represent the limiting fluxes assumed for the source extraction.

components found by the clean algorithm, we flagged any residual visibilities still affected by interference. Then we performed the deconvolution on the new visibility data-set (after having recombined the previously subtracted components). Self-calibration was used to make additional corrections to the antenna gains as a function of time, to improve the image quality and to account for the fact that interpolated calibrator gains do not determine the antenna gains perfectly at each time step.

To minimise the side-lobes of bright off-field sources, we performed a few iterations of the cleaning algorithm on a double-sized (four times in area) low resolution image of the field, subtracting the components found in the external parts of the image from the visibility file. The final images were obtained by adding the components found by the deconvolution algorithm to the residual image. This was done with the task RESTOR. Once good quality images of each field were obtained, we constructed the final mosaics using the linear combination task LINMOS (which also corrects for primary beam attenuation). Two mosaics were first created for each of the two frequency bands and then added, resulting in a square $2^\circ \times 2^\circ$ mosaic with almost uniform sensitivity over the full region. Figure 2 exhibits a grey scale image of the total mosaic of the entire S1 area.

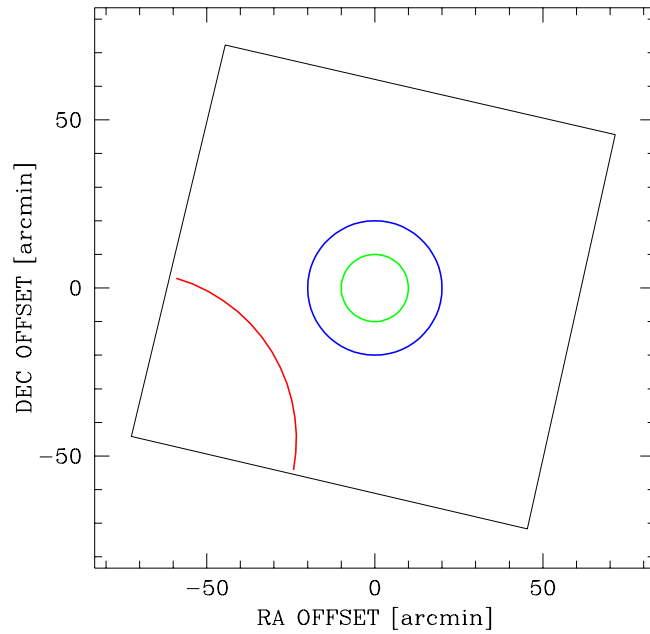


Figure 4. Regions of different average rms noise defined for source extraction. The radii of the circles are 10, 20 and 50 arcmin for the central inner, the central outer and corner circles respectively, and the corresponding rms noise is 40 μJy , 60 μJy and 100 μJy . The rest of the field has a constant rms of 80 μJy .

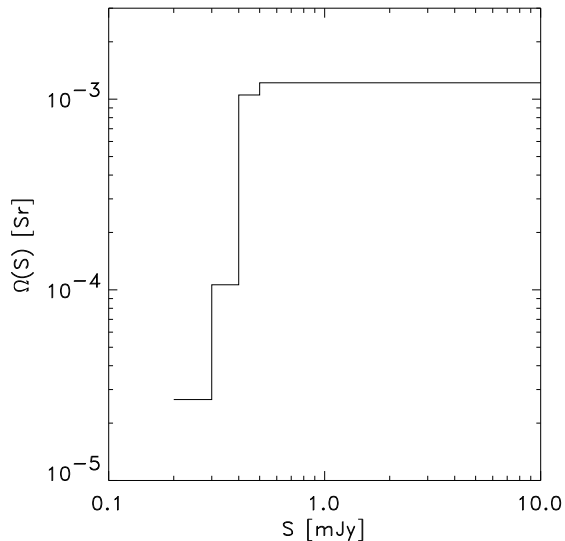


Figure 5. Areal coverage of S1 field represented by the solid angle over which a source with peak flux S can be detected.

3.1 Noise distribution in the mosaic

The amplitude distribution of pixel values in the final mosaic corresponds to an almost Gaussian noise core plus a positive tail due to actual sources. The standard deviation of the Gaussian which fits the distribution is $\sim 80 \mu\text{Jy}$, almost coincident with the theoretical rms value expected in the image. However, as is clearly visible in figure 2, the bright,

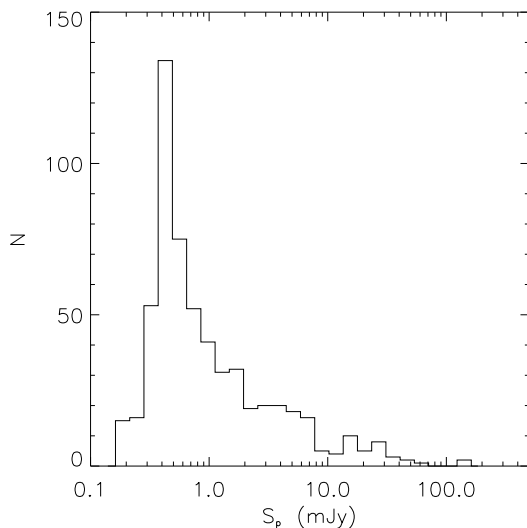


Figure 6. Distribution of peak flux densities for radio sources of the S1 1.4 GHz complete sample.

extended source PMNJ0042-4413 located just outside the field of interest was strong enough (above 1 Jy) to produce sidelobes and hence limit the dynamic range over a part of the mosaic.

To deal with this problem, we analyzed the noise properties in the image as a function of radial distance along two diagonals of the square defined by the S1 field. In figure 3 we plot the variations of the rms noise with distance from the field center along the diagonal not affected by the sidelobes of PMNJ0042-4413 (top panel) and along the one degraded by them (bottom panel). Except in the corner disturbed by PMNJ0042-4413, where the rms noise is obviously higher than expected, the rms noise in the mosaic is uniform over most of the image. It is smaller in the center where a longer integration has been obtained, and almost flat over most of the survey area. Using figure 3 we defined regions with different but uniform levels of rms noise to characterise the sensitivity for source extraction. We adopted a 1σ sensitivity of $40 \mu\text{Jy}$ in a circular area of 10 arcmin radius in the field center; $60 \mu\text{Jy}$ in a $10 < r < 20 \text{ arcmin}$ annulus; $100 \mu\text{Jy}$ in the area delimited by a 50 arcmin radius circle centered on the noisy corner and two sides of S1; and $80 \mu\text{Jy}$ over the rest of the field. Figure 4 illustrates the location and extent of these regions.

Using these sensitivities we obtained the integral distribution of the rms noise in the image and the detectability area as a function of flux density. In figure 5 the solid angle $\Omega(S)$ over which a source with a peak flux density S can be detected is plotted as a function of flux density. The ‘step’ structure of the areal coverage is due to the fact that the field is divided in separate regions of constant rms noise.

4 THE SOURCE CATALOGUE

4.1 Source detection

The criterion for including a source in the catalogue is that its peak flux density is ≥ 5 times the average rms value

in its region of the image. Source extraction was performed using the MIRIAD task IMSAD (Image Search and Destroy), which searches for islands of pixels above a given cutoff and attempts to fit Gaussian components to the islands. Source parameters, derived by least-squares bi-dimensional Gaussian fitting, are the right ascension and declination of the island centroid, peak flux density, integrated flux density, deconvolved (from the beam) major axis full width at half maximum FWHM (arcsec), deconvolved minor axis FWHM (arcsec) and deconvolved position angle (degrees).

As discussed by Condon (1997), the results of Gaussian fitting can be unreliable for sources with low signal-to-noise ratios. Thus, we used IMSAD to extract all the sources whose peak flux, S_p , was greater than 4 times the local rms value and then, for sources with $4\sigma < S_p \leq 7\sigma$, we derived the peak flux density by second degree interpolation (task MAXFIT) and the total flux density by integrating the image value in a rectangle around the source. Only sources with a MAXFIT peak flux density $\geq 5\sigma$ were included in the final sample. For the other parameters (major axis, minor axis and position angle) we retained the values given by IMSAD.

4.2 The catalogue

Our method selected 581 sources with peak flux density $\geq 5\sigma$, over an area of 4 deg^2 . Of these, 31 appear to have two or more components. Figure 6 illustrates the distribution of peak flux density for the 581 sources in the catalogue. This distribution shows that the majority of the radio sources in our sample ($\sim 60\%$, 349/581) have peak flux density in the sub-mJy region. Thus, our data-set provides a large and statistically significant sub-sample of radio sources fainter than 1 mJy.

We have considered as potential doubles all the sources separated by less than about twice the FWHM of the synthesized beam ($\sim 30 \text{ arcsec}$) and having approximately equal flux densities in the two components (ratio ≤ 2.5). For triple or multiple sources the distance between each component and the probable nucleus has been considered, while the flux density ratios have been computed between the various components excluding the nucleus. All the components satisfying the adopted criteria have been assumed to form a unique, multiple source. Figure 7 shows contour images of the sources classified as double or multiple in the catalogue.

The catalogue contains a total of 621 components, and reports the source name, the peak flux density S_p (in mJy), the integrated flux density S_t (in mJy), the source position (right ascension and declination at equinox J2000), the FWHM of the major and minor axes, the positional angle of the major axis, the signal-to-noise ratio and a character as a comment about the deconvolution outcome (D=deconvolution of source size from beam OK, P=deconvolution gave result close to point source, F=deconvolution failed, E=multiple source). Whenever the deconvolution of the source size from the beam failed (F), the fitted parameters (instead of the deconvolved ones) are reported in the catalogue. For double or multiple sources the components are labeled ‘A’, ‘B’, etc., followed by a line labeled ‘T’ in which parameters for the total source are given. The position of the total source has been computed as the flux-weighted average position for all the components. In Table 1 the first page of the catalogue is shown

Table 1: The ATCA 1.4-GHz Radio Catalog of S1

Name	S_p (mJy)	σ_{S_p} (mJy)	S_t (mJy)	σ_{S_t} (mJy)	RA (J2000)	DEC (J2000)	σ_α (η)	σ_δ (η)	θ_M (η)	θ_m (η)	PA (deg)	σ_{θ_M} (η)	σ_{θ_m} (η)	σ_{PA} (deg)	SNR	C
ELAISR20_J002830-424456A	7.182	0.083	13.080	0.151	0 28 28.69	-42 44 52.0	0.146	0.341	10.890	7.404	7.233	0.256	0.106	0.001	89.8	D
ELAISR20_J002830-424456B	5.400	0.082	11.530	0.174	0 28 31.01	-42 45 01.5	0.179	0.347	14.120	7.471	138.700	0.379	0.136	0.001	67.5	D
ELAISR20_J002830-424456T	-	-	21.780	0.230	0 28 29.69	-42 44 56.1	0.176	0.360	-	-	-	-	-	-	-	E
ELAISR20_J002830-425102	7.071	0.078	7.429	0.082	0 28 30.34	-42 51 01.5	0.141	0.337	3.988	1.264	2.681	0.228	0.067	0.001	88.4	D
ELAISR20_J002830-425349	0.500	0.079	0.598	0.094	0 28 30.43	-42 53 49.4	0.698	1.433	16.870	8.564	21.730	3.516	1.021	0.019	6.3	P
ELAISR20_J002835-424822	0.416	0.083	0.577	0.114	0 28 35.26	-42 48 22.0	1.223	1.449	16.850	9.948	39.070	4.077	1.619	0.048	5.2	P
ELAISR20_J002837-424528A	1.179	0.080	1.233	0.084	0 28 36.11	-42 45 35.1	0.282	0.597	14.460	8.679	17.340	1.230	0.469	0.005	14.7	P
ELAISR20_J002837-424528B	2.510	0.078	2.932	0.091	0 28 37.70	-42 45 24.0	0.195	0.425	16.810	8.339	22.890	0.701	0.193	0.001	31.4	P
ELAISR20_J002837-424528T	-	-	4.185	0.124	0 28 37.19	-42 45 27.6	0.333	0.564	-	-	-	-	-	-	-	E
ELAISR20_J002840-425746	0.455	0.077	0.492	0.083	0 28 39.52	-42 57 46.4	0.547	1.595	14.624	7.002	9.270	3.751	1.002	0.020	5.7	D
ELAISR20_J002846-425132	6.822	0.077	7.011	0.080	0 28 45.59	-42 51 32.2	0.152	0.333	2.935	0.413	37.520	0.232	0.068	0.001	85.3	D
ELAISR20_J002850-430155	1.025	0.075	0.929	0.068	0 28 49.87	-43 01 54.5	0.287	0.673	14.470	7.515	18.050	1.457	0.404	0.004	12.8	F
ELAISR20_J002854-431218	3.567	0.077	3.726	0.081	0 28 54.18	-43 12 17.9	0.188	0.357	3.702	0.424	39.090	0.450	0.129	0.001	44.6	D
ELAISR20_J002856-430556	0.383	0.073	0.361	0.069	0 28 56.32	-43 05 58.2	0.568	1.548	13.710	7.020	14.400	3.672	0.951	0.025	5.0	F
ELAISR20_J002909-432922	1.111	0.077	0.967	0.067	0 29 09.02	-43 29 21.8	0.260	0.574	13.030	8.011	14.900	1.151	0.440	0.006	13.9	F
ELAISR20_J002912-431434	0.841	0.077	0.988	0.091	0 29 12.44	-43 14 33.8	0.610	0.763	7.126	1.622	40.010	2.073	0.555	0.006	10.5	D
ELAISR20_J002916-432638	4.683	0.078	4.949	0.083	0 29 15.53	-43 26 38.4	0.186	0.334	2.813	1.873	59.130	0.336	0.104	0.001	58.5	D
ELAISR20_J002916-430335	0.516	0.077	0.447	0.067	0 29 15.81	-43 03 35.1	0.684	1.173	14.823	7.888	27.597	2.960	0.879	0.018	6.1	F
ELAISR20_J002918-432422	1.081	0.077	0.995	0.071	0 29 18.09	-43 24 22.4	0.303	0.613	14.030	7.870	22.340	1.315	0.426	0.005	13.5	F
ELAISR20_J002922-425544	27.700	0.079	30.970	0.088	0 29 21.54	-42 55 43.6	0.139	0.324	4.607	2.696	40.970	0.058	0.018	0.001	346.3	D
ELAISR20_J002928-431614	2.893	0.079	2.987	0.082	0 29 27.71	-43 16 14.2	0.164	0.387	14.690	8.436	13.100	0.515	0.180	0.001	36.2	F
ELAISR20_J002931-431141	0.611	0.078	0.561	0.072	0 29 30.69	-43 11 41.2	0.404	0.967	13.420	8.205	9.435	2.172	0.831	0.020	7.6	F
ELAISR20_J002932-434227	1.619	0.081	1.692	0.084	0 29 32.13	-43 42 26.6	0.241	0.472	14.080	8.909	22.030	0.860	0.362	0.003	20.2	F
ELAISR20_J002933-431516	1.043	0.080	1.110	0.086	0 29 33.28	-43 15 15.5	0.314	0.654	14.500	8.809	17.260	1.391	0.545	0.007	13.0	F
ELAISR20_J002933-434314	0.403	0.078	0.350	0.067	0 29 33.28	-43 43 13.7	0.668	1.461	13.968	8.048	162.860	3.492	1.196	0.038	5.0	F
ELAISR20_J002934-430811	2.491	0.077	2.447	0.076	0 29 34.05	-43 08 11.2	0.179	0.407	14.870	7.928	19.530	0.615	0.184	0.001	31.1	F
ELAISR20_J002938-434447	1.032	0.078	1.059	0.080	0 29 37.63	-43 44 46.6	0.279	0.696	14.960	8.233	12.810	1.485	0.478	0.005	12.9	P
ELAISR20_J002938-432946	0.644	0.077	0.810	0.097	0 29 38.22	-43 29 46.4	0.856	0.883	6.714	0.590	-45.910	2.683	0.703	0.010	8.1	D
ELAISR20_J002945-424142	0.429	0.081	0.438	0.083	0 29 45.31	-42 41 41.8	0.693	1.317	13.640	8.975	16.160	3.104	1.401	0.057	5.4	F
ELAISR20_J002946-432149	7.324	0.076	14.980	0.156	0 29 45.78	-43 21 48.8	0.187	0.324	14.190	2.981	-89.970	0.298	0.064	0.001	91.6	D
ELAISR20_J002947-431554	24.110	0.079	26.580	0.087	0 29 46.52	-43 15 54.3	0.140	0.324	3.646	2.648	62.830	0.066	0.021	0.001	301.4	D
ELAISR20_J002951-440551A	2.563	0.078	2.542	0.077	0 29 49.86	-44 05 41.2	0.166	0.402	14.450	8.147	11.090	0.573	0.191	0.001	31.0	F
ELAISR20_J002951-440551B	4.419	0.079	4.401	0.078	0 29 51.20	-44 05 56.4	0.149	0.351	14.440	8.278	13.500	0.331	0.114	0.001	55.2	F
ELAISR20_J002951-440551T	-	-	5.663	0.110	0 29 50.71	-44 05 50.8	0.205	0.409	-	-	-	-	-	-	E	

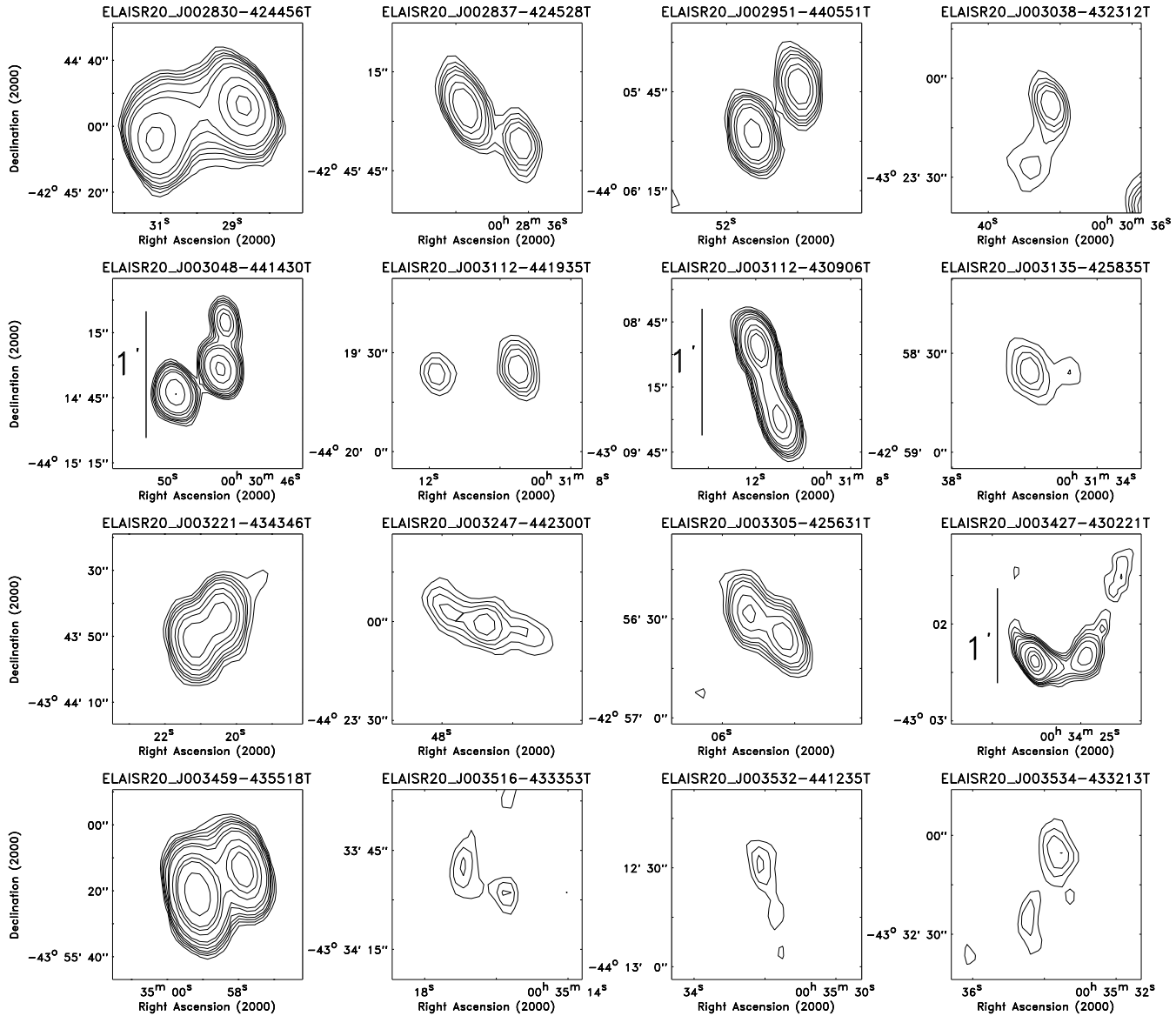


Figure 7. Contour images of the 31 radio sources classified as double or multiple in S1. The contour levels are at 3, 4.5, 6, 7.5, 10, 20, 40, 60, 80, 160, 320, 640 times the local rms value for all the sources.

as an example. The full catalogue will be available from <http://athena.ph.ic.ac.uk/>.

4.3 Errors in the source parameters

The formal relative errors determined by a Gaussian fit are generally smaller than the true uncertainties of the source parameters. Gaussian random noise often dominates the errors in the data (Condon 1997). Thus, we used the Condon (1997) error propagation equations to estimate the true errors on fluxes, axes and position angle:

$$\frac{\sigma_{S_p}^2}{S_p^2} = \frac{\sigma_{S_t}^2}{S_t^2} = \frac{\sigma_{\theta_M}^2}{\theta_M^2} = \frac{\sigma_{\theta_m}^2}{\theta_m^2} = \frac{\sigma_{PA}^2}{2} \left(\frac{\theta_M^2 - \theta_m^2}{\theta_M^2 \theta_m^2} \right)^2 = \frac{2}{\rho^2} \quad (2)$$

where S_p and S_t are the peak and the total fluxes, θ_M and θ_m the fitted FWHMs of the major and minor axes, PA is the position angle of the major axis (the σ s are the relative errors) and ρ is the signal-to-noise ratio, given by

$$\rho^2 = \frac{\theta_M \theta_m}{4\theta_N^2} \left[1 + \left(\frac{\theta_N}{\theta_M} \right)^2 \right]^{\alpha_M} \left[1 + \left(\frac{\theta_N}{\theta_m} \right)^2 \right]^{\alpha_m} \frac{S_p^2}{\sigma_{map}^2} \quad (3)$$

where σ_{map} is the noise variance of the image and θ_N is the FWHM of the Gaussian correlation length of the image noise (\simeq FWHM of the synthesized beam). The exponents are $\alpha_M = 5/2$ and $\alpha_m = 1/2$ for calculating σ_M , $\alpha_M = 1/2$ and $\alpha_m = 5/2$ for calculating σ_m and σ_{PA} and $\alpha_M = \alpha_m = 3/2$ for the flux densities. These two equa-

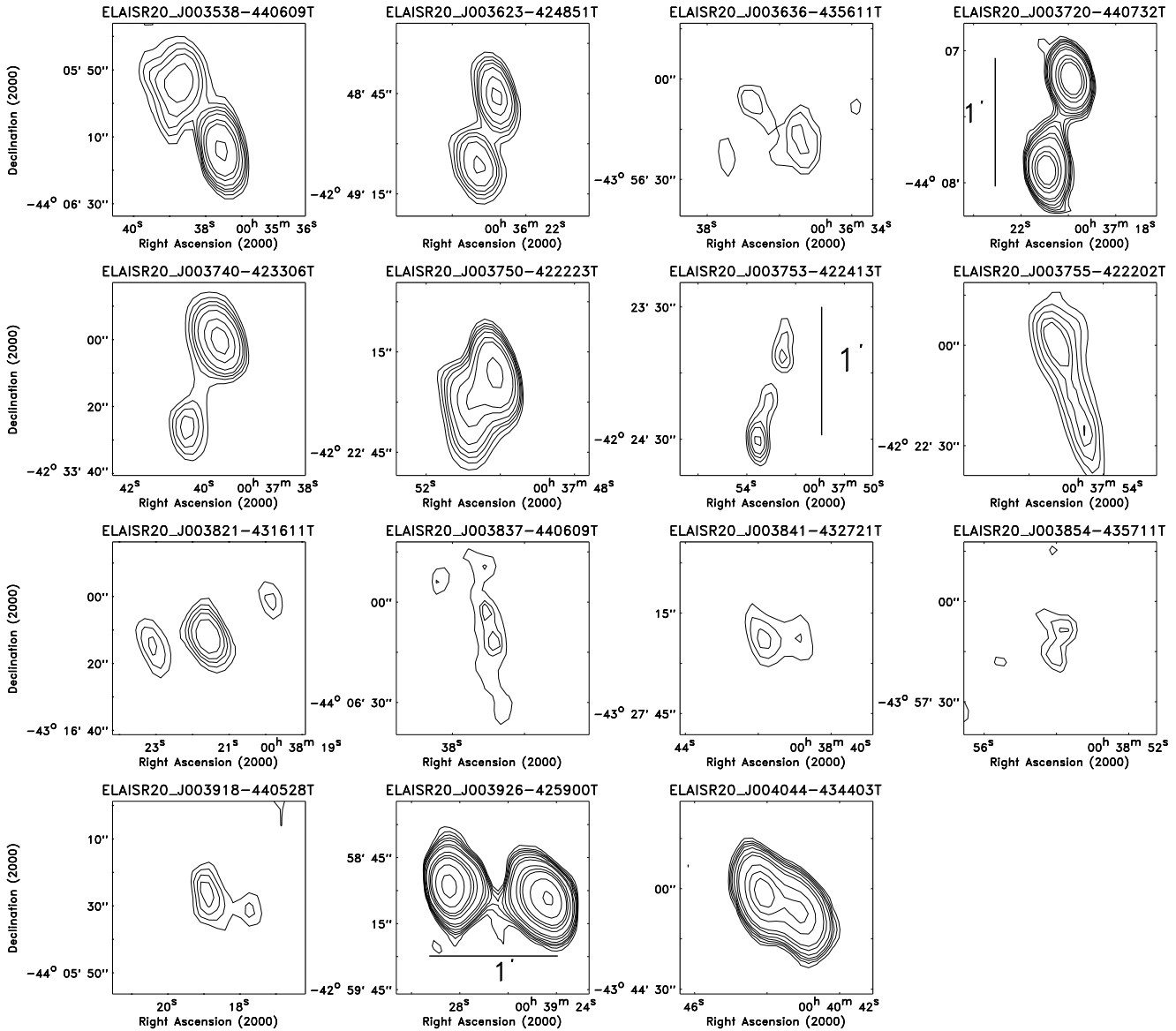


Figure 7 – continued

tions are the master equations for estimating the variance in the parameters derived from a two-dimensional Gaussian fit. The projection of the major and minor axis errors onto the right ascension and declination axes produces the total rms position errors given by Condon et al. (1998)

$$\sigma_{\alpha}^2 = \varepsilon_{\alpha}^2 + \sigma_{x_0}^2 \sin^2(PA) + \sigma_{y_0}^2 \cos^2(PA) \quad (4)$$

$$\sigma_{\delta}^2 = \varepsilon_{\delta}^2 + \sigma_{x_0}^2 \cos^2(PA) + \sigma_{y_0}^2 \sin^2(PA) \quad (5)$$

where $(\varepsilon_{\alpha}, \varepsilon_{\delta})$ are the ‘‘calibration’’ errors, while σ_{x_0} and σ_{y_0} are $\theta_M^2/(4\ln 2)\rho^2$ and $\theta_m^2/(4\ln 2)\rho^2$ respectively.

Calibration errors cannot be determined from the survey image alone. They can be determined from comparison with accurate positions of sources strong enough that the noise terms in equation 4 and 5 are much smaller than the

calibration terms. Because S1 area is covered by no other 1.4-GHz radio catalogue suitable for estimating the calibration errors, we have used our data to derive the mosaic errors. This internal check gives only a lower limit on the source position errors. However, Hopkins et al. (1998) have used Monte Carlo methods to explore source-fitting uncertainties in ATCA mosaiced images with statistical properties similar to those of the images discussed here. Their study implies that the positional errors are rarely as large as 2 arcsec, and more typically lie below 1 arcsec.

The mosaic map contains several overlapping regions where sources are detected in two different pointings. We have run IMSAD on each single pointing map (after having corrected for the primary beam shape), considering the sources detected as an independent data set. Then we used

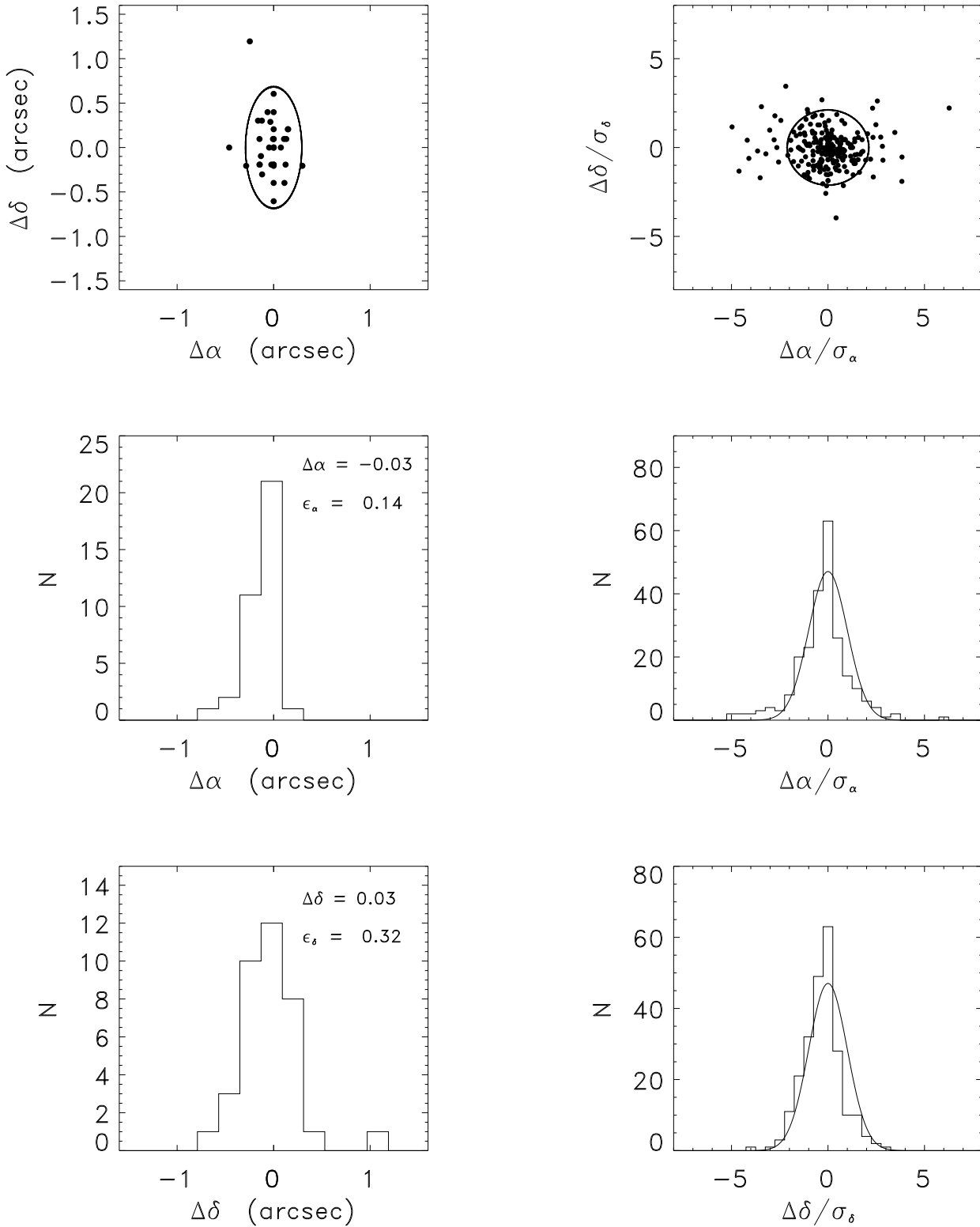


Figure 8. Position errors for 36 bright single sources ($S > 10$ mJy) common to two individual pointing images composing the mosaic image. In the *top panel* the semi-axes of the 90% confidence ellipse shown are $(2 \ln 10)^{1/2}$ times the rms errors ($\epsilon_\alpha, \epsilon_\delta$) = ($0''.138, 0''.323$).

Figure 9. Position errors for 236 weak single sources (fainter than 10 mJy) in the overlapping regions, in units of the combined position uncertainties ($\sigma_\alpha, \sigma_\delta$). In the *top panel* the 90% confidence error circle is plotted. The smooth curves in the *central* and *lower panels* represent the expected Gaussian of zero mean and unit variance.

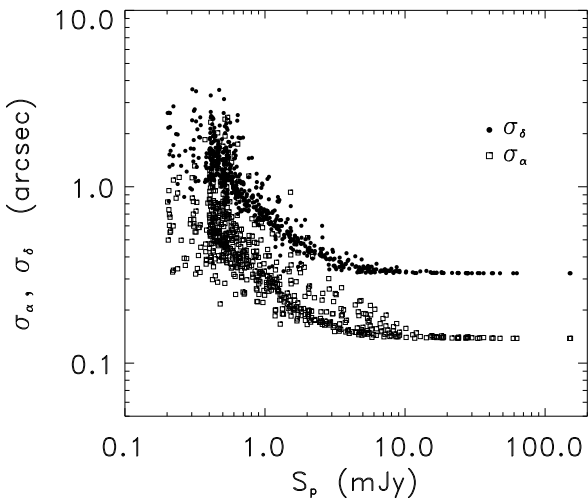


Figure 10. Rms position uncertainties σ_α and σ_δ for all the single sources of peak flux S_p in our catalogue.

the sources in common between two different pointing maps to estimate the positional errors. First we used 36 sources brighter than 10 mJy to calculate the mean image offsets and the mosaic uncertainties. Their offsets $\Delta\alpha$ and $\Delta\delta$ are shown in figure 8. The mean offsets of our mosaic map are $\langle \Delta\alpha \rangle = -0.^{\circ}027 \pm 0.^{\circ}029$ and $\langle \Delta\delta \rangle = 0.^{\circ}031 \pm 0.^{\circ}059$. Due to the negligible values of these image offsets, the source positions in the catalogue have not been corrected for them. The offset distributions (reported in figure 8) indicate the mosaic position errors of our data, which are $\varepsilon_\alpha = 0.^{\circ}138$ in right ascension and $\varepsilon_\delta = 0.^{\circ}323$ in declination.

Positional uncertainties for all sources have been calculated according to equations 4 and 5, adopting the mosaic errors derived using the 36 sources brighter than 10 mJy. To verify that these uncertainties are realistic, especially at low flux densities where the noise and confusion components dominate the errors, we used the 236 sources fainter than 10 mJy in the overlapping regions and found their position offsets. Figure 9 shows these offsets ($\Delta\alpha$, $\Delta\delta$) normalized by the combined uncertainties (σ_α , σ_δ), where $\sigma_\alpha^2 = \sigma_{\alpha 1}^2 + \sigma_{\alpha 2}^2$ and $\sigma_\delta^2 = \sigma_{\delta 1}^2 + \sigma_{\delta 2}^2$ with $\sigma_{\alpha 1}$, $\sigma_{\alpha 2}$, $\sigma_{\delta 1}$ and $\sigma_{\delta 2}$ being the errors on the single measurements from equations 4 and 5). As shown in figure 9, where the expected Gaussians are plotted over our normalized offset distributions, the normalized offset have nearly zero mean and unit rms scatter, verifying that our catalogue uncertainties are accurate also for weak sources. Many of these sources are slightly extended, so our catalogue positional errors for weak sources include possible offsets between the source centroids and cores. In extended sources, there might be an intrinsic offset between the fitted centroid position and the real radio core position.

The rms position uncertainties (σ_α , σ_δ) of all the sources in our catalogue are plotted as functions of peak flux in figure 10.

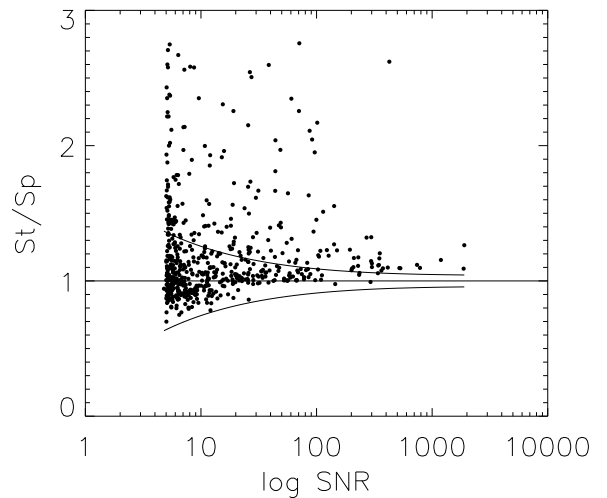


Figure 11. The measured ratio of integrated to peak flux as a function of signal-to-noise ratio for the S1 ATCA survey. The upper line defines the upper envelope of the S_t/S_p distribution containing the sources that we have considered unresolved.

5 SOURCE COUNTS

The sample of 581 sources with $S_p \geq 5\sigma$ has been used to construct the source counts distribution. Complex sources or sources with multiple components have been treated as a single radio source. Every source was weighted for the reciprocal of its detectability area (figure 5), defined as the area over which the source could have been seen above the adopted threshold of 5σ (Katgert et al. 1973).

An estimate of the extension of a source can be obtained from the ratio of the integrated flux density to the peak flux density S_t/S_p . Figure 11 shows that the ratio has a skew distribution, with a tail towards high flux density ratios, especially when the signal-to-noise ratio is low. To establish a criterion for extendedness, we have determined the upper envelope of the distribution of S_t/S_p containing the unresolved sources. The solid lines drawn in figure 11 represent the best-fit curves to the upper and lower envelopes of the band containing all the sources considered to be unresolved. For these sources we have adopted the peak flux in computing the source counts, while for all the others, lying above the upper envelope, we have adopted the total flux.

In Table 2 the 1.4 GHz source counts are presented. The columns give the adopted flux density intervals, the average flux density in each interval computed as the geometric mean of the two flux limits, the observed number of sources in each flux interval, the differential source density (in $\text{sr}^{-1} \text{Jy}^{-1}$), the normalized differential counts $nS^{2.5}$ (in $\text{sr}^{-1} \text{Jy}^{1.5}$) with estimated errors (as $n^{1/2}S^{2.5}$) and the integral counts (in sr^{-1}).

The 1.4 GHz differential source counts of the ATCA data, normalized to those expected in a Euclidean geometry by dividing by $S^{-2.5}$, are shown in figure 12 (filled stars). For comparison, source counts from other surveys are also plotted. The solid line represents the model of Windhorst, Mathis & Neuschaefer (1990) obtained by fitting counts from 24 different 1.4 GHz surveys, while the open circles are the

Table 2. The 1.4 GHz ATCA Radio Source Counts

S (mJy)	$\langle S \rangle$ (mJy)	N_s	$n = dN/dS$ (sr $^{-1}$ Jy $^{-1}$)	$nS^{2.5}$ (sr $^{-1}$ Jy $^{1.5}$)	$N(> S)$ (sr $^{-1}$)
0.20–0.36	0.27	29	4.53×10^9	5.3 ± 1.0	7.24×10^5
0.36–0.65	0.48	182	1.50×10^9	7.7 ± 0.6	4.31×10^5
0.65–1.17	0.87	128	2.56×10^8	5.7 ± 0.5	1.32×10^5
1.17–2.10	1.57	84	7.40×10^7	7.2 ± 0.8	6.91×10^4
2.10–3.78	2.82	49	2.39×10^7	10.1 ± 1.4	4.02×10^4
3.78–6.80	5.07	42	1.14×10^7	20.9 ± 3.2	3.45×10^4
6.80–12.2	9.13	25	3.77×10^6	30.0 ± 6.0	2.05×10^4
12.2–22.0	16.5	18	1.51×10^6	52.2 ± 12.3	1.48×10^4
22.0–39.7	29.6	15	6.98×10^5	105.0 ± 27.1	1.23×10^4
39.7–71.4	53.2	5	1.29×10^5	84.5 ± 37.8	4.10×10^3
71.4–128.5	95.8	3	4.31×10^4	122.4 ± 70.7	2.46×10^3
128.5–231.4	172.5	2	1.60×10^4	197.1 ± 139.4	1.64×10^3

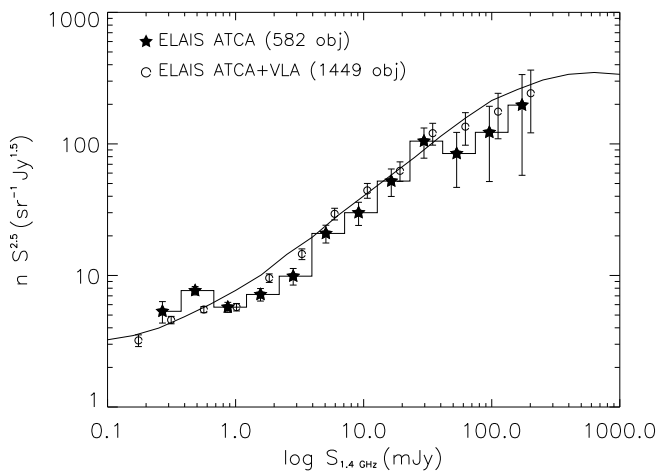


Figure 12. The 1.4 GHz normalized differential source counts for the ELAIS ATCA data. The abscissa gives the flux density (mJy) and the ordinate gives the differential number of sources normalized by $S^{2.5}$ (sr $^{-1}$ Jy $^{1.5}$). The solid line represents the model of Windhorst, Mathis & Neuschaefer (1990) obtained by fitting counts from 24 different 1.4 GHz surveys. The filled stars are the counts obtained from our ATCA data in the ELAIS southern region, while the open circles are the total radio counts in the ELAIS regions obtained by combining the S1 data with the VLA in the northern ELAIS regions (Ciliegi et al. 1998).

total counts obtained by combining the S1 data with the VLA data in the northern ELAIS regions (Ciliegi et al. 1998). Our counts agree with those obtained by previous surveys and confirm the upturn observed by several authors below about 1 mJy, considered as the characteristic feature of the ‘sub-mJy population’.

A maximum likelihood fit to both our ATCA and ATCA+VLA 1.4 GHz counts with two power laws:

$$\frac{dN}{dS} \propto \begin{cases} S^{-\alpha_1} & \text{if } S > S_b \\ S^{-\alpha_2} & \text{if } S < S_b \end{cases} \quad (6)$$

gives the following parameters: $\alpha_1 = 1.73 \pm 0.11$, $\alpha_2 = 3.04 \pm 0.27$, $S_b = (0.72 \pm 0.23)$ mJy and $\alpha_1 = 1.74 \pm 0.06$, $\alpha_2 = 2.48 \pm$

0.11, $S_b = (0.53 \pm 0.13)$ mJy, respectively. Although the errors for the ATCA data only are relatively large, in both cases our best fit parameters suggest that the re-steepening of the integral counts toward an Euclidean slope starts just below ~ 1 mJy, in agreement with the recent results of Gruppioni et al. (1997) and Ciliegi et al. (1998). By contrast, in previous work (Windhorst et al. 1985, 1990), a best-fit value of 5 mJy had been derived for the flux density at which the change in slope of the source counts occurs.

6 CONCLUSIONS AND FUTURE PLANS

This paper presents a 1.4 GHz survey obtained with the ATCA of the European Large Area ISO Survey (ELAIS) region S1 located in the southern celestial hemisphere. A mosaic of forty-nine separate observations with different pointing positions has provided an image with low and uniform rms noise over the whole S1 area (~ 4 deg 2). The lowest 5σ flux density reached by our observation is 0.2 mJy, while the bulk of the imaged area has a 5σ flux density limit of 0.4 mJy.

The observations provide a large, complete sample of 581 sources (with peak flux greater than 5σ), the majority of which have flux densities in the sub-mJy range. We have constructed the differential source counts over the flux range 0.2–200 mJy. Our counts agree with the results from other deep 1.4 GHz surveys (Windhorst et al. 1990; Gruppioni et al. 1997; Ciliegi et al. 1998) and confirm the change in slope observed below ~ 1 mJy.

This survey of the southern ELAIS field, S1, will be combined with the VLA survey of the northern fields, N1, N2 and N3 (Ciliegi et al. 1998), and deep multi-waveband data (optical and near-, mid- and far-infrared) in the same area, to investigate the nature of the sub-mJy population. Moreover, due to the accurate radio positions, the radio sample will play a crucial role in the optical identification phase of the ISO program.

Spectroscopic observations for about 350 radio/ISO sources in S1 have recently been obtained (end of September 1998) with the Anglo Australian Telescope (AAT) Two Degrees Field Spectrograph (2dF). These observations will provide crucial information about the spectroscopic nature

and the redshift distribution of our objects, and allow estimation of the obscured star formation rate with two highly complementary samples, selected in the infrared and radio within the same volume of Universe. In fact, since the radio luminosity traces the supernovae associated with star formation regions and is not affected by dust obscuration, independent estimates of the star formation rate for sources with reliable distance indications can also be calculated on the basis of radio flux density measurements (see Oliver et al. 1998).

ACKNOWLEDGMENTS

This paper is based on observations collected at the Australia Telescope Compact Array (ATCA), which is funded by the Commonwealth of Australia for operation as a National Facility by CSIRO. CG thanks Isabella Prandoni for useful suggestions on mosaic data reduction strategies and Neil Killeen for assistance in using the ATNF facilities at Epping and for kindly providing the data tapes in a readable form. LC and AH acknowledge support from the Australia Research Council. This work was supported by the EC TMR Network program FMRX-CT96-0068.

REFERENCES

Benn C.R., Rowan-Robinson M., McMahon R.G., Broadhurst T.J. & Lawrence A., 1993, MNRAS, 263, 98

Cesarsky C., et al., 1996, A&A, 315, L32

Ciliegi P., McMahon R.G., Miley G., Gruppioni C., Rowan-Robinson M., Cesarsky C., Danese L., Franceschini A., Genzel R., Lawrence A., Lemke D., Oliver S., Puget J-L., Rocca-Volmerange B., 1998, MNRAS, in press

Condon J.J., 1992, ARA&A, 30, 575

Condon J.J., 1997, PASP, 109, 166

Condon J.J., Cotton W.D., Greisen E.W., Yin Q.F., Perley R.A., Taylor G.B. & Broderick J.J., 1998, AJ, 115, 1693

Cram L., Hopkins A., Mobasher B. & Rowan-Robinson M., 1998, MNRAS, in press (astro-ph/9805327)

Griffith M.R. & Wright A.E., 1993, AJ, 105, 1666

Gruppioni C., Zamorani G., de Ruiter H.R., Parma P., Mignoli M. & Lari C., 1997, MNRAS, 286, 470

Gruppioni C., Mignoli M. & Zamorani G., 1998, MNRAS, in press

Hammer F., Flores H., Lilly S., Crampton D., Le Fèvre O., Rola C., Mallen G., Schade D., Tresse L., 1997, ApJ, 481, 49

Helou G., Soifer B.T. & Rowan-Robinson M., 1985, ApJL, 298, L7

Hopkins A., Mobasher B., Cram L. & Rowan-Robinson M., 1998, MNRAS, 296, 839

Katgert P., Katgert-Merkelijn J.K., Le Poole R.S. & van der Laan H., 1973, A&A, 23, 171

Lemke D., et al., 1994, *ISOPHOT Observer's Manual*, U. Klaas, H. Krueger, I. Heinrichsen, H. Heske, R. Laureijs eds. ESA Pubs.

Oliver S., Gruppioni C. & Serjeant S., 1998, MNRAS, submitted (astro-ph/9808260)

Oliver S. et al., 1997, in B. McLean ed., Proc. of IAU Symp. 179, New Orizons from Multiwavelength Sky Surveys. Kluwer, Dordrecht, in press

Prandoni I., 1997, PhD Thesis, University of Bologna

Richards E.A., Kellermann K.I., Fomalont E.B., Windhorst R.A. & Partridge R.B., 1998, ApJ, in press (astro-ph/9803343)

Rowan-Robinson M., Benn C.R., Lawrence A., McMahon R.G. & Broadhurst T.J., 1993, MNRAS, 263, 123

Sault R.J. & Killeen N.E.B., 1995, *MIRIAD Users Guide*.

Sault R.J. & Wieringa M.H., 1994, A&AS, 108, 585

Sault R.J., Staveley-Smith L. & Brouw W.N., 1996, A&AS, 120, 375

Windhorst R.A., Mathis D.F. & Neuschaefer L.W., 1990, in Kron R.G., ed., ASP Conf. Ser. Vol. 10, Evolution of the Universe of Galaxies. Bookcrafters, Provo, p. 389

Windhorst R.A., Miley G.K., Owen F.N., Kron R.G. & Koo D.C., 1985, ApJ, 289, 494

Windhorst R.A., Fomalont E.B., Kellermann K.I., Partridge R.B., Richards E., Franklin B.E., Pascale S.M. & Griffiths R.E., 1995, Nature, 375, 471